Lawrence Berkeley National Laboratory
LBL Publications

Title
Polysulfide-Permanganate Flow Battery Using Abundant Active Materials

Permalink
https://escholarship.org/uc/item/6tz6r8gw

Journal
Journal of The Electrochemical Society, 168(7)

ISSN
0013-4651

Authors
Yang, Zhiwei
Gerhardt, Michael R
Fortin, Michael
et al.

Publication Date
2021-07-01

DOI
10.1149/1945-7111/ac1036

Peer reviewed

Polysulfide-Permanganate Flow Battery Using Abundant Active Materials

Polysulfide-Permanganate Flow Battery Using Abundant Active Materials

Zhiwei Yang,[1] Michael R. Gerhardt,[2] Michael Fortin,[1] Christopher Shovlin,[1] Adam Z. Weber,[2,*] Mike L. Perry,[3,*] Robert M. Darling,[1,**] and James D. Saraidaridis[1,**,z]

[1]*Raytheon Technologies Research Center, East Hartford, Connecticut 06118, United States of America*
[2]*Energy Conversion Group, Energy Technologies Area, Lawrence Berkeley National Laboratory, Berkeley, California 94720, United States of America*
[3]*Flow Cell Tech LLC, Groton, Connecticut 06340, United States of America*

A new flow battery is presented using the abundant and inexpensive active material pairs permanganate/manganate and disulfide/tetrasulfide. A wetted material set is identified for compatibility with the strongly oxidizing manganese couple at ambient and elevated temperatures. Both solutions allow high active material solubility, with cells tested at theoretical energy densities up to 43 Wh l^{-1} for the ~1.2 V cell. Full cells built with nickel foam electrodes and sodium-exchanged Nafion 115 membranes deliver a baseline area-specific resistance of 2.7 Ω-cm^2. Incorporation of high-surface-area cobalt-coated carbon paper and high-surface-area stainless steel mesh electrodes, and an expanded Nafion 115 membrane delivers cells with 44% lower resistance at 1.6 Ω-cm^2. All cells show performance decay over the course of cycling. The Co-decorated carbon paper electrodes provide significant kinetic improvements, shifting electrode performance from non-linear with Ni-foam to linear with a volume-normalized exchange current density value of 3.2 A cm^{-3}. The expanded membrane provides increased conductivity over the 13 mS cm^{-1} conductivity observed in as-received, sodium-exchanged Nafion 115. Although boiled membranes provide improved conductivity, it is at the cost of decreased Coulombic efficiency and poorer manufacturability. Full cell models suggest that similar cell resistances (1.7 Ω-cm^2) should be feasible with as-received Nafion 115 and advanced electrodes.
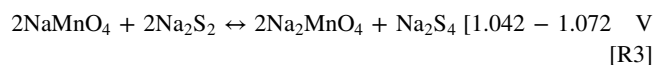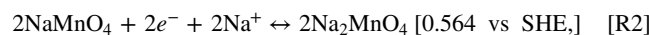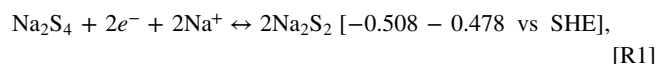
The increasing grid market-share of renewable electricity generators rely on resources like wind turbines and solar photovoltaics, whose generation is determined by environmental conditions rather than by electricity demand. For an electric grid powered completely by these low-cost, but intermittent, resources, planners would need to address the inability to actively manage electricity generation. One strategy is to overbuild the generator resource (i.e. turbines and solar photovoltaic arrays) power capacity and curtail generation at times when it outpaces demand. An alternative is to incorporate energy storage into an overbuilt generation grid and store electricity at times of low demand, for disbursement at times of high demand. The specific implementation will depend on the details of the grid and its generator resource mix, but strategies that incorporate energy storage can achieve significantly higher CO_2 emission reductions as well as more efficient use—via higher capacity factors—of renewable generators.[1]

Energy storage capacity on the grid is presently dominated by pumped-hydroelectric storage, but the past decade has brought increasing adoption of electrochemical energy storage (EES) such as Li-ion batteries and redox flow batteries (RFBs).[2,3] As more storage gets added to the grid, policymakers have recognized the need for systems with longer durations (that is, greater energy storage relative to system rated power delivery), and have sought systems that can provide durations of 8+ h.[3–5] At these longer durations, redox flow batteries have an advantage over Li-ion systems since the incremental cost of another hour of installed duration asymptotes to the cost of additional active materials and their storage containers, rather than additional cells, packs and modules.

Leading vanadium flow batteries have made progress in RFB cost reduction by improving the power density of their energy conversion stacks,[6,7] but eventually are limited by the relatively high, incremental cost of vanadium. Switching to lower cost active materials can permit economically feasible long duration flow battery systems.[8] The proposed sulfur-manganese chemistry uses abundant, low cost sulfur, a waste product of fossil fuel production, and abundant, inexpensive manganese, presently used commercially in disposable primary cells. Annual production of sulfur and manganese, individually, are three-orders-of-magnitude higher than the annual production of vanadium and the same order-of-magnitude of its world reserves.[9–11]

The S-Mn RFB described herein relies on polysulfide (pS) reactions nominally ranging between the disulfide and tetrasulfide species for the negative electrolyte as described in Reaction 1. Equilibrium between the various polysulfide chain lengths in alkaline media suggest that species ranging from sulfide to pentasulfide likely exist in solution.[12,13] The positive electrolyte relies on the permanganate—manganate reaction couple in strongly alkaline media as described in Reaction 2.[14,15]

$$Na_2S_4 + 2e^- + 2Na^+ \leftrightarrow 2Na_2S_2 \; [-0.508 - 0.478 \; \text{vs SHE}], \quad [R1]$$

$$2NaMnO_4 + 2e^- + 2Na^+ \leftrightarrow 2Na_2MnO_4 \; [0.564 \; \text{vs SHE,}] \quad [R2]$$

$$2NaMnO_4 + 2Na_2S_2 \leftrightarrow 2Na_2MnO_4 + Na_2S_4 \; [1.042 - 1.072 \; \text{V}] \quad [R3]$$

Although the formal cell potential of 1.1 V, as described in Reaction 3, is relatively low compared to the leading vanadium chemistry (~1.5 V), the solubility of these active materials is high. Full cell results demonstrated below are performed at 2.1 and 2.7 M—corresponding to energy densities of 30 and 40 Wh l^{-1}, respectively, for a 1.1 V chemistry. Higher energy densities are achievable by extending the window of allowable nominal polysulfide chain length, but that is not addressed in this paper.

*Electrochemical Society Fellow.
**Electrochemical Society Member.
zE-mail: James.Saraidaridis@rtx.com

Experimental

Soaking experiments—stability.—All cell materials expected to have battery solution exposure were tested for compatibility with the aqueous supporting electrolyte and battery solutions: 3 M sodium hydroxide (NaOH, 50 wt% in water, Fisher Chemical); 2.1 M sodium sulfide nonahydrate (Na$_2$S, 98+%, ACS reagent, ACROS organics) and 2.1 M sulfur (S, 99.5%, Alfa Aesar) in 3 M NaOH; and 2.1 M sodium permanganate (NaMnO$_4$, 40 wt% in water, Sigma-Aldrich) in 3 M NaOH. Material samples were massed and visually inspected before immersing in 40 ml of the battery solutions and stored in a polypropylene centrifuge tube. Control soaking experiments containing no wetted materials were simultaneously generated and stored. The stability of the materials were assessed by their resulting mass, physical appearance, and comparison of the state-of-charge (SOC) or pH of the electrolytic solution that they were stored in against the SOC of the control samples.[16] SOC of the manganese electrolyte was measured using ultraviolet-visible spectroscopy (UV–vis, Cary 4000) on diluted (1000×) aliquots of the battery electrolyte solutions and calculated using characteristic wavelengths of 437 nm (manganate), 508 nm (permanganate), and 571 nm (isosbestic) for the sodium permanganate/manganate couple. The polysulfide electrolyte has some apparent dependence on SOC between the disulfide to tetrasulfide species, but a clear method to convert changes in UV–vis absorbance method to a reliable SOC calculation was not found. The manganese SOC, as determined ex situ with UV–vis, has parallels to the SOC estimated via coulomb-counting from battery electrolytes *in operando*:

$$SOC = \frac{Cap_{theory} - Cap_{disch}}{Cap_{theory}} \quad [1]$$

The SOC of battery solutions were tested after initial preparation, after 1 week of soaking, and after 3 weeks of soaking. Soaking tests were performed at both ambient and elevated (60 °C) temperatures.

Cell configurations.—Flow cell experiments were carried out in custom single cell flow battery hardware with 21.6 cm^2 flow-field area, which has been used by the authors for vanadium redox flow battery testing in the past.[17–20] The membrane was sandwiched between negative and positive electrodes, and then assembled between two graphite (Tokai G347B, Tokai Carbon Co., Ltd., Japan) or stainless steel 316 blocks that both had superimposed interdigitated flow fields (IDFF) unless otherwise specified.[17] The inlet and outlet were configured for co-current flow of reactant electrolytes.

Nafion®-115 (Ion Power Inc., Delaware, USA) was used as the membrane in full cells and sodiated in one of two processes: soaking the as-received membrane in 3 M NaOH solution for 3+ days (AR-Na N115); or boiling the as-received membrane in deionized water for 1 h before soaking in 3 M NaOH solution for 3+ days (B-Na N115). Nickel foam (Ni foam, 1.6 mm, MTI Corporation) and Dutch-weave stainless steel mesh (DW SS, 165 × 800, 0.003″ & 0.002″ wire diameters, McMaster-Carr) were used as received. Cobalt decorated carbon paper (Co-CP) was prepared by using heat-treated "Carbon paper A", which the authors have reported on previously.[17–20] The heat treatment consisted of heating to 400 °C in air for 30 h. The heat-treated carbon paper was decorated with cobalt catalyst according to the reported method[21] to give a cobalt loading of ~5 mg cm^{-2}.

Double-half-cells (DHCs) also used the AR-Na N115 membrane, and were constructed with a single layer, or as part of a membrane thickness study, using multiple layers. The thickness study also included a Nafion-212 membrane prepared in the previously described as-received sodiation method (AR-Na N212). DHCs built as part of the membrane thickness study included 0.3 mm-thick polypropylene mesh (110 × 110 mesh, McMaster-Carr) between the electrodes and membranes to prevent errant measurements caused by possible electrode short-circuits through the membrane(s).

The different cell membranes and electrode materials tested in this study are summarized in Table I.

Electrochemical performance tests.—All cells were subjected to charge/discharge cycling in order to quantify their electrochemical performance, in terms of round-trip voltage efficiency (VE), columbic efficiency (CE) and energy efficiency (EE). The tests started with electrolyte volumes of 30 or 40 ml per side that were circulated by two diaphragm pumps (NF-10, KNF Neuberger, NJ) that provide 110 ± 10 ml min^{-1} flow rates. The cell temperature was maintained at 50 °C. The starting negative electrolyte contained 2.1 M Na$_2$S-9H$_2$O, 2.1 M S, in 3.0 M NaOH and the starting positive electrolyte contained 2.1 M of NaMnO$_4$ in 3.0 M NaOH, unless otherwise noted. The charge/discharge cycling was conducted galvanostatically at 28 mA cm^{-2} until the cell voltage reached 0.7 V on discharge, or until the cell received 1.35 A-hr input capacity on charge, which corresponds to 60% of the theoretical electrolyte capacity. Cycling tests were controlled by a multi-channel potentiostat (Model BT2000, Arbin Instrument Inc., College Station, TX). Electrochemical impedance spectroscopy (EIS) measurements were carried out by a Solartron 1287 interface and a Solartron 1255B frequency analyzer. The impedance spectra were collected at frequencies from 100 kHz to 1 Hz using 5-mV perturbation and no DC voltage bias.

Modeling.—A two-dimensional cross-sectional model of the cell was developed in COMSOL Multiphysics 5.5 based on a prior framework used by the authors.[22] The model domain consisted of an ion-exchange membrane sandwiched between two porous electrodes and spans from the center of an inlet channel to the center of an adjacent outlet channel. A sketch of the model domain is shown in Fig. 1. For a complete description of the model, including specific equations and material properties, see the Supplemental Information; a summary of the model follows. Fluid flow through the porous electrodes was modeled with Darcy's Law. Ion flux within the electrolyte was calculated with the Nernst-Planck equation. The rate of the manganate-permanganate reaction was modeled with a Butler-Volmer reaction rate expression. The polysulfide redox reaction was modeled as a two-electron reduction from S$_4^{2-}$ to 2S$_2^{2-}$ using a Butler-Volmer reaction rate expression. This simplified approach resulted in good fits to the polysulfide DHC data but neglects some of the complexities in polysulfide speciation. Model fits to the DHC data for both the manganate-permanganate and polysulfide electrode reactions are shown in Fig. S1 (available online at stacks.iop.org/JES/168/070516/mmedia). The reduction potential of the polysulfide electrode was estimated by calculating the equilibrium polysulfide speciation at a given SOC using the free energies of formation of the known aqueous polysulfide species S$_2^{2-}$ through S$_5^{2-}$, HS$^-$, and S^{2-}, as discussed in Kelsall and Thompson.[12] Constant pressure and concentration boundary conditions were used at the inlets, and the pressure at the inlet was set to achieve the average flow rate expected from experimental conditions. At the outlet, the pressure was set to ambient. To generate a polarization curve, a constant current boundary condition was applied at the positive electrode/land interface, the potential was set to zero at the negative electrode/land interface, and the current was gradually increased while recording the computed voltage.

Results and Discussion

Wetted material stability.—In efforts to deliver practical cell voltages, redox couples selected for RFBs often operate at voltages that can readily cause side reactions. Strongly negative couples can lead to hydrogen generation as observed with the chromium couple in iron-chrome systems,[23] or strongly positive couples can lead to carbon or membrane oxidation as evidenced with vanadium systems.[24] The sulfur-manganese system described herein uses strongly alkaline conditions (3 M NaOH) and the strongly oxidative permanganate-manganate couple. The permanganate-manganate

Table I. The cell configurations for the results reported herein.

| Cell	Negative Electrode	Membrane	Positive Electrode	Comments
Ni-foam	MTI Ni Foam	AR-Na N115	MTI Ni Foam	Baseline
Ni foam pS	MTI Ni Foam	AR-Na N115	MTI Ni Foam	Baseline pS DHC
Co-CP pS	Co-coated carbon paper	1,2,3x AR-Na N115 & N212	Co-coated carbon paper	Advanced pS DHC and membrane thickness study
Ni Mn DHC	MTI Ni Foam	AR-Na N115	MTI Ni Foam	Baseline Mn DHC
SS Mn DHC	DW SS mesh	1,2,3x AR-Na N115 & N212	DW SS mesh	Advanced Mn DHC and membrane thickness study
Ni-free	Co-coated CP	AR-Na N115	DW SS mesh	Advanced electrodes
Metal—contact	Co-coated CP	AR-Na N115	DW SS mesh	SS‖SS FF-electrode contact
Expanded N115	Co-coated CP	B-Na N115	DW SS mesh	Boiled membrane
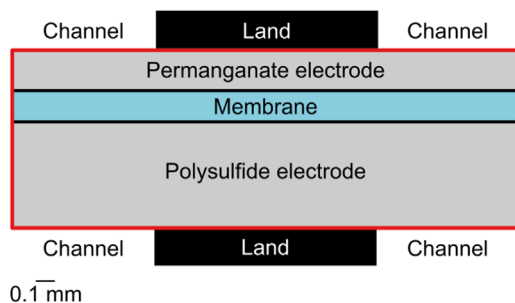
Figure 1. A sketch showing the model domain. The model domain is bounded by the red box and comprises the permanganate electrode, membrane, and polysulfide electrodes. The boundary conditions are varied along the outer electrode edges to capture the effects of the channel and the land.

couple has a standard reaction potential of 0.564 V vs the standard hydrogen electrode (SHE),[13] which, at pH 14.5, is 194 mV higher than the hydroxide oxidation reaction. The polysulfide chemistry is not as extreme—the reaction potential for the disulfide/trisulfide couple and trisulfide/tetrasulfide couple are -0.508 V and -0.478 V vs SHE, respectively.[13] These polysulfide species are meta-stable under alkaline conditions and appear in predominance diagrams when sulfoxy species are excluded.[12] At pH 14.5 these polysulfide reactions occur at more positive reaction potentials than the hydrogen evolution reaction, thereby avoiding potential hydrogen-generating side reactions.

Arising from the strongly oxidative nature of the permanganate active species, this active material suffers from self-discharge reactions that can lead to spontaneously decreasing solution SOCs absent any foreign oxidizable materials in solution.[14,15]

$$4\,MnO_4^- + 4\,OH^- \leftrightarrow 4\,MnO_4^{2-} + 2\,H_2O + O_2 \qquad [R4]$$
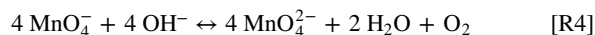
This self-discharge is observed in the control sample's decreasing SOC with shelf time as shown in Table II. Self-discharge occurs more rapidly in solutions stored at elevated temperatures compared than those stored at ambient temperatures.

To understand the stability of the wetted materials used in a cell, and possible impacts on cell performance, the SOC of the manganese battery electrolytes were monitored in the presence of wetted material. Wetted materials are listed in Table II along with SOCs of positive battery electrolytes with soak time. Soaking wetted materials in negative battery electrolyte or supporting electrolyte solutions showed no evidence of degradation with time as observed by solution SOC or pH or material appearance and are therefore not reported here.

The non-conductive material set tested at high temperature shows stability in the highly oxidative, strongly alkaline positive electrolyte. Notably, these solutions required replacing Viton tubing in the default cell build with FEP-lined vinyl tubing. Although not included in Table II, Viton tubing showed evidence of degradation at ambient temperatures: lower solution SOCs than the control sample, and bulk material embrittlement and discoloration.

The conductive material set, which included possible electrode materials and flow plate/current collector materials, showed increased solution discharge compared to the non-conductive materials initially, but the rate slowed significantly from week 1 to week 3. The nickel foam electrode material showed the slowest discharge rate of the conductive materials and was closest to the discharge rate of non-conductive materials. The stainless steel 316 mesh and graphite flow plate material both showed significantly faster self-discharge rates in the first week than non-conductive materials, but slowed significantly between week 1 and week 3, to the point that both soaking solutions remained within 10% of the control SOC by the end of 3 weeks. Visual inspection of the conductive materials showed yellow-brown staining on the surface of the metal electrode materials, and roughened, darkened discoloration of the graphite flow plate material.

As indicated by the control sample, the self-discharge rate appears to slow with decreasing electrolyte SOC. Downward-drifting solution potential as the electrolyte self-discharges may be responsible for the slowing rates on self-discharge at high SOCs (i.e. the Nernst curve is steep at high SOCs). However, the slowing of self-discharge from moderately high SOCs to middling SOCs would require the reaction mechanism to be extremely sensitive to potential in this region. There may be other effects that factor into self-discharge rates in this SOC range. Upon reaching more middling SOCs, the conductive wetted materials appear to stabilize relative to what is observed with the non-conductive materials and pristine battery solution. The more rapid self-discharge of solutions in contact with the conductive materials must be considered for cells that can deliver high SOC positive electrolytes.

Baseline cell performance using Ni foam electrodes.—Porous nickel foam was reported to effectively catalyze the polysulfide redox reaction,[25,26] and also can support the permanganate reduction reaction at reasonably high rates.[14] The first polysulfide—permanganate (pS-Mn) flow battery cell is demonstrated using Ni foam as both anode and cathode electrodes and AR-Na N115 as membrane. Starting with 40 ml of positive and negative electrolytes and active material reactant concentrations of 2.1 M corresponded to a theoretical capacity of 2.25 A-hr under the assumption of one electron per one redox active molecule in the charged state (MnO_4^-, or S_2^{2-}).

Figure 2a shows the cell voltage profile during the initial discharge at 28 mA cm^{-2}. The total discharge capacity reached

Table II. Wetted material stability testing results.

|	2.1 M NaMnO$_4$, 3 M NaOH		
	SOC		
Sample at 50 °C	0 weeks	1 week	3 weeks
Control	0.98	0.73	0.57
Nafion 115 membrane	0.98	0.72	0.56
Polypropylene barb fittings	0.98	0.72	0.54
Fluorinated ethylene propylene tubing liner	0.98	0.74	0.57
Pump diaphragm material	0.98	0.73	0.57
Stainless Steel 316 mesh electrode	0.98	0.58	0.49
Ni Foam electrode	0.98	0.69	0.51
Graphite Flow Plate	0.98	0.65	0.49
Sample at ambient (25 °C)			
25 °C Control	1.00	0.93	0.84
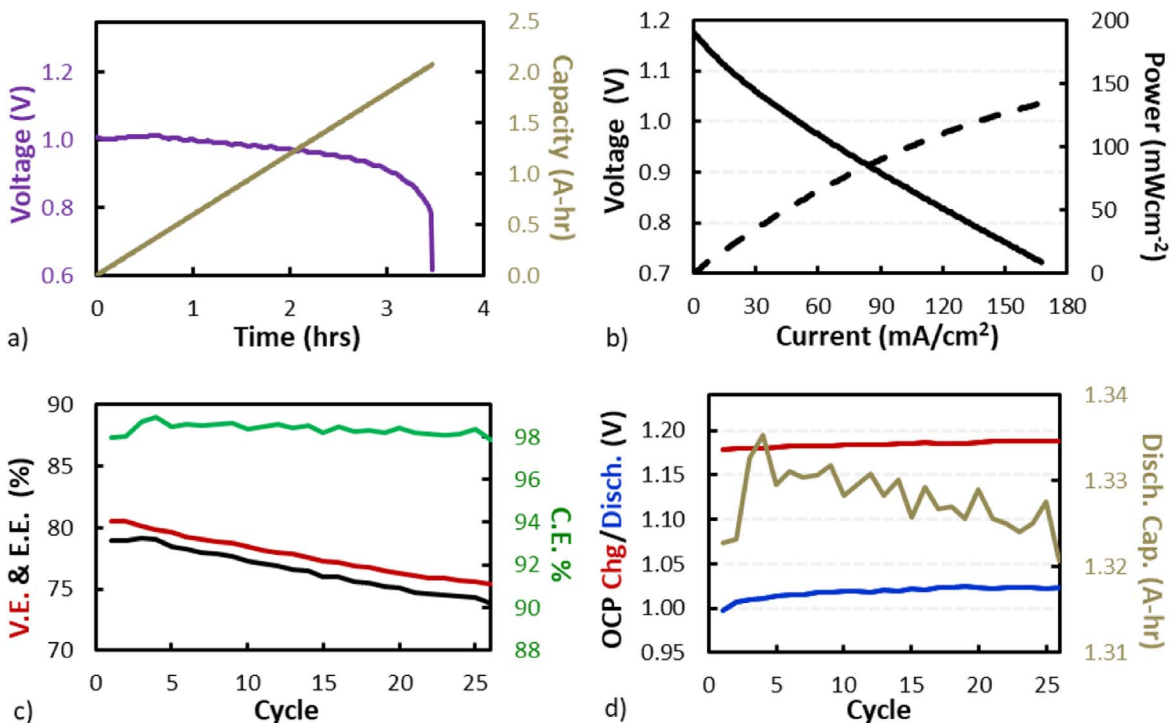
Figure 2. Baseline Ni-foam Cell (MTI Ni foam || AR-Na N115 || MTI Ni foam) run with 40 ml of 2.1 M actives, 3 M NaOH battery solutions; (a) initial discharge voltage profile and discharge capacity, (b) polarizaton curve at 50% SOC, (c) cycling efficiencies, (d) discharge capacity and OCP at the end of charge and discharge.

2.05 A-hr before hitting the 0.7 V discharge cutoff criteria. According to Eq. 1, used to calculate SOC, this discharging step brought the electrolyte to 10% SOC. The cell was then charged at 28 mA cm^{-2} to deliver 1.35 A-hr of charge capacity, corresponding to 60% of the theoretical electrolyte capacity. Absent side reactions or crossover, this would be expected to charge the electrolytes up to 70% SOC. Figure 2b shows the polarization curve of the cell taken after discharge to 50% SOC as assessed by coulomb-counting. To keep the SOC relatively constant during the entire polarization curve, the measurement was run quickly using a current-staircase scan at a rate of 9.25 mA cm^{-2} per second from open circuit voltage (OCP) to 186 mA cm^{-2} or a minimum cell voltage of 0.7 V. The discharge area specific resistance (ASR) of the cell was measured to be ~2.7 Ω-cm^2 by calculating the slope of the polarization curve in the current density range of 20 ∼ 50 mA cm^{-2}. Previous modeling suggests flow cell polarization performance losses arise mainly from three factors, electrode kinetic overpotentials, mass transport overpotentials, and ohmic overpotentials.[27] The polarization curve in Fig. 2b appears to be approximately linear, especially at higher current density values, indicating the mass transport may not be a significant issue in the present case. Electrode kinetic and ohmic resistance, including membrane resistance, appears to be key factors contributing to ASR.

Upon completion of the polarization experiment, the cell was discharged until its voltage reached 0.7 V, and normal cycling across the 10%–70% SOC window resumed. The cell cycled successfully over the remaining programmed 26 cycles. Figure 2c shows the cycling performance in terms of voltaic, coulombic, and energy efficiency (VE, CE, and EE, respectively) over 26 cycles operating at a cell temperature of 50 °C. The cell exhibited excellent VE (> 80%) at the beginning of life (BOL), which decreased to 75.5% after 26 cycles. CE was approximately 98% and decreased marginally (< 1% after 26 cycles). This gave an E.E of 79% at BOL that decreased to 74% by the end of the test. The VE loss with cycles suggests possible deterioration of electrode performance and/or increasing ohmic cell resistance, since both can lead to the increases in the cell's charge/discharge overpotential. Manganese precipitation

can explain both deterioration pathways and can occur either by exposure to sufficiently reducing conditions as illustrated by the predominance diagram in Fig. S2 or by disproportionation. Reducing conditions can be generated either by crossover of polysulfide active materials as well as reducing electrode potentials on the positive electrode during discharge. Precipitation can also arise from sequential disproportionation reactions of MnO_4^{2-}, which occurs at extremely low rates in strongly alkaline conditions:[14]

$$3MnO_4^{2-} + 2H_2O \rightarrow 2MnO_4^- + MnO_2 + 4OH^- \qquad [R5]$$
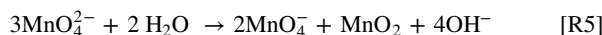
Precipitation can therefore occur both in the membrane and at the positive electrode. Disassembly of cycled cells confirmed the presence of precipitate in the membrane and positive electrode, but not in the negative electrode. This phenomenon, along with mitigation techniques to remove and recover precipitated manganese will be discussed in future communications.

Observing the OCP in the rest holds after charge and discharge steps, as illustrated in Fig. 2d, allows one to deconvolute contributions to the performance decay from phenomena that require active current, such as electrode activity or increased membrane or contact resistance, from passive contributions, such as side-reaction-induced changes in electrolyte SOC. Cycling led to increasing discharge overpotentials as illustrated by slightly higher OCPs upon conclusion of discharge (blue line in Fig. 2d), as well as slightly lower discharge capacities (tan line in Fig. 2d). The corresponding increase in OCP at the end of charge, indicates that electrolyte SOC mismatch is not playing a role here. Instead the fading VE arises from a cell that is developing increased internal resistance.

Nickel-free full cell performance with advanced electrodes.— The initial cells built with Ni foam electrodes show promising performance. Nickel foam, however, is both a departure from the material set often used in flow battery manufacturing, and also an expensive, potentially resource-constrained metal in a specialty morphological format. Symmetric double-half-cells (DHCs) and full cells built with alternative catalytic electrodes examined the

role of alternative electrodes in the cell's charge/discharge performance. Cobalt-decorated carbon fiber paper is reported to be a highly effective catalytic electrode for the polysulfide redox reaction.[21,25] While cobalt has its own material concerns and constraints, shifting to a decorated carbon paper paradigm greatly reduces the mass of the critical material in use. On the positive electrode, nickel foam is replaced with a finely woven stainless steel mesh. This format permits a similar cell or stack construction paradigm (e.g. thin 2-dimensional electrode material, rather than thicker, increasingly 3-dimensional foam) yet the fine mesh maintains a high electrode surface area.

Polysulfide DHCs using 50% SOC electrolyte and built with the high surface-area cobalt catalyst decorated carbon paper (Co-CP) show superior performance compared to the DHC built with Ni foam electrodes. Polarization curves included in Fig. 3a qualitatively show the advancement toward nearly linear kinetics in the cell built with Co-CP, whereas the Ni foam cells show exponential kinetic behavior. Furthermore, the Co-CP showed improved performance compared to pristine heat-treated carbon papers, which were also non-linear (not shown). As illustrated in Fig. 3a, the area specific resistance of the double half-cell at low overpotentials dropped from 6.95 Ω-cm^2 to 1.96 Ω-cm^2 by switching from Ni foam to Co-CP.

For manganese DHCs, the Ni foam and Dutch-weave SS mesh electrodes deliver similar performance when tested using 50% SOC electrolyte. Polarization curves in Fig. 3b show linear kinetics for both electrodes and indicate the more facile nature of the permanganate/manganate reaction kinetics compared to the polysulfide electrolyte. The Ni foam DHC shows incrementally lower resistance

than the DW SS, suggesting faster kinetic capabilities with Ni materials. The switch to DW SS was largely motivated by avoidance of a specialty metal product with a different form factor than electrodes often used with the inter-digitated flow fields employed in these cells.

Finally, Mn and pS DHCs built with 1–3 layers of AR-Na N115 or a single layer of similarly pre-treated AR-Na N212 allow comparison of the membrane ohmic resistance in the two DHC environments. These cells, built with Co-CP or DW SS electrodes and their membrane layers protected from possible shorting by a polypropylene mesh, show similar high frequency resistance (HFR) dependence on thickness of the Nafion membrane layer. EIS-based HFR measurements provide measurements of the ohmic-behaving resistances in the cell e.g. contact resistance, membrane ionic conductivity. According to the slopes shown in Fig. 3c, both the pS and Mn DHCs indicate, and predict for full cells, a membrane conductivity of 13 mS cm^{-1} for the 127-um-thick Nafion 115 membrane layer when immersed in the 3M-NaOH-supported battery solutions. Both sets of cells indicate a high non-membrane ohmic resistance ranging from 0.6–0.7 Ω-cm^2, but this arises largely due to the addition of the pP-mesh between the electrodes and membrane for these experiments.

An improved, nickel-free, full cell was built using the advanced negative electrode consisting of two layers of Co-CP, one layer of DW SS as the positive electrode, and an AR-Na N115 membrane. Figure 4a compares the initial discharge and subsequent charge profile (at 28 mA cm^{-2}) between the Ni-foam and Ni-free cells. The Ni-free cell shows noticeably higher cell voltage than the Ni-foam
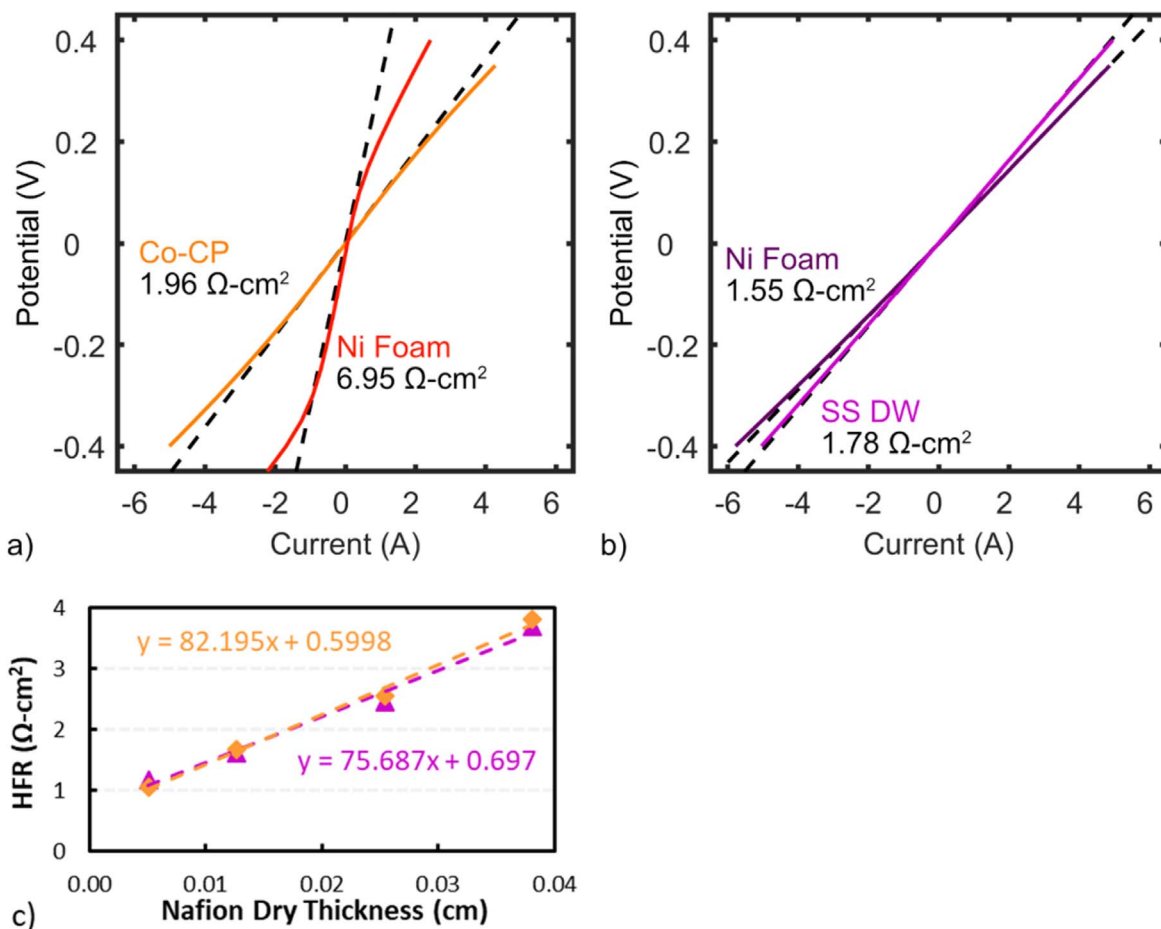

Figure 3. Polarization curves at 50 °C using 2.1 M active solutions in 3 M NaOH: 50% SOC of: (a) polysulfide DHCs built with Ni foam or 2× Co-CP electrodes on both sides of an AR-Na N115 membrane; (b) manganese DHCs built with Ni foam or SS DW electrodes on both sides of an AR-Na N115 membrane. (c) EIS-based HFR measurements of pS and Mn DHCs built with varying thicknesses of Nafion membrane and using 2.7 M active solutions in 3 M NaOH.
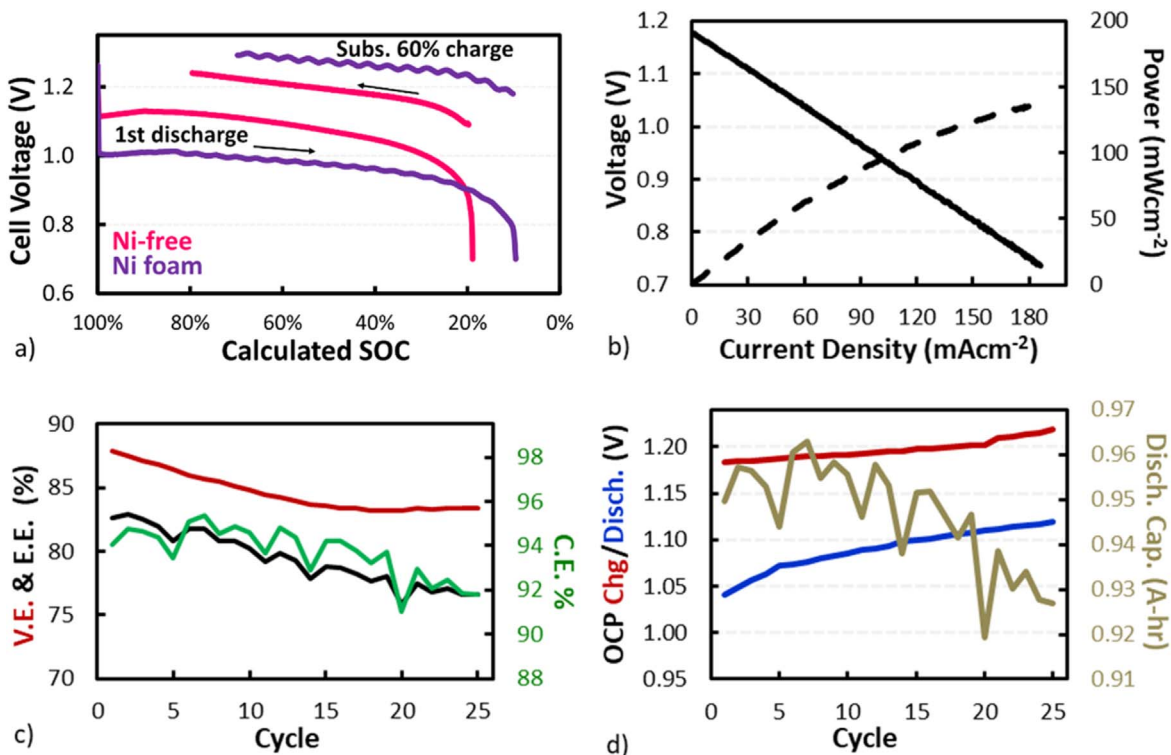
Figure 4. Ni-free Cell (2× Co-decorated Carbon paper A || AR-Na N115 || DW SS 316 mesh) run with 30 ml of battery solutions: (a) initial discharge voltage profile and subsequent charging voltage profile (b) polarizaton curve at 50% SOC (c) cycling efficiencies, (d) OCP collected at the end of change and discharge.

cell across most of the discharge profile, indicating that rate capabilities of the new electrodes are better than the Ni foam. An additional difference arose during the initial discharge: the voltage across the Ni-free cell began to decrease quickly and reached the 0.7 V discharge cutoff at a theoretical SOC of ∼20% at the end of discharge. This is a 10% discharge capacity reduction compared to the Ni-foam cell under the same conditions.

The improved rate capabilities of the advanced electrodes in these cells stand in contrast to the lower capacity performance. However, there are a couple of expected contributions to this lowered discharge capacity in the Ni-free cell. As shown in the material stability analysis in Table II, this decreased capacity can be partly explained by the use of SS electrodes, which lead to more rapid self-discharge at high permanganate/manganate electrolyte SOCs than observed with the Ni foam material. After one week of soaking, the difference between SS and Ni is 11%, indicating that a 10% SOC difference between cells using the different electrode materials is possible, though likely pushing the upper-bound over a much shorter time-scale. Other phenomena may also contribute to the lower capacity.

Another expected contribution arises from the electrode architecture and its impacts on mass transfer at lower SOCs. The two layers of cobalt-decorated carbon paper in the cell have a total thickness of 0.42 mm and 85% porosity. The stainless steel 316 mesh positive electrode is 0.16 mm thick and has 51% porosity. Compare this to the Ni foam electrodes, which are 1.6 mm thick and have >95% porosity. While the morphological differences in electrode likely contribute, further examination of their contributions will be considered in subsequent communications.

The Ni-foam and Ni-free cell's subsequent charging profile are included in Fig. 4a. Similar to the discharging step, the overpotentials for the Ni-free cell operation are significantly lower and indicated the higher rate capabilities of the Co-decorated carbon paper paired with SS mesh. This increased electrode performance manifests in the polarization curve shown in Fig. 4b, as a more linear polarization that gives a full cell ASR of 2.4 Ω-cm^2.

As expected, the Ni-free cell, with lower overpotentials across a complete charge/discharge cycle than that of the Ni foam cell, showed significantly higher VE at BOL, 88% (Fig. 4c). Despite improved efficiency, the Ni-free cell still suffers from the same performance fade as the Ni-foam cell: VE decreases with cycling and the OCP measured at the end the of charge and discharge steps drifts higher with cycles (Fig. 4d). The Ni-free cell also shows evidence of deteriorating CE with cycling, decaying from ∼94% at BOL to 92% at the end of test (EOT). Despite using the same membrane material and preparation, the CE of the Ni-free cell is generally lower than what was observed in the Ni-foam cell, indicating that there may be side reactions or other root causes responsible for the lower CE and its decay with cycling. The decrease in both VE and CE of the Ni-free cell led to the cell's EE decreasing from 83% at the BOL to be 76.5% after 26 cycles.

This decay in the Ni-free cell is larger than the decay in Ni foam cell despite the same number of cycles. EE fade could be due to many factors, including changes in electrode activity, membrane resistance and contact resistance between different materials.

Comparing the resting OCP data illustrated in Figs. 2d and 4d indicates slightly higher OCP values at the end of discharge in the Ni-free cell. The Ni-free cell is experiencing higher overpotentials at end of discharge than the Ni foam cell and points to mass transfer limitations as the major cause for lower initial capacity observed in Fig. 4a, rather than more rapid permanganate self-discharge on the DW SS electrode.

Further comparison of the Ni foam and Ni free cycling performance and OCP data indicates that the decay in VE shown in Figs. 2c and 4c is likely induced by similar precipitation phenomena. The decreasing CE and faster-increasing OCP of the Ni-free cell in Figs. 4c and 4d (compared to Figs. 2c and 2d) indicates that this system is undergoing additional impacts. In the Ni-free construction, the cell relies on compression between the SS mesh electrode and the graphite flow field to provide low contact resistance between the SS mesh and the graphite flow plate—the current path relies on tangential contact between the graphite flow field and SS wires in a
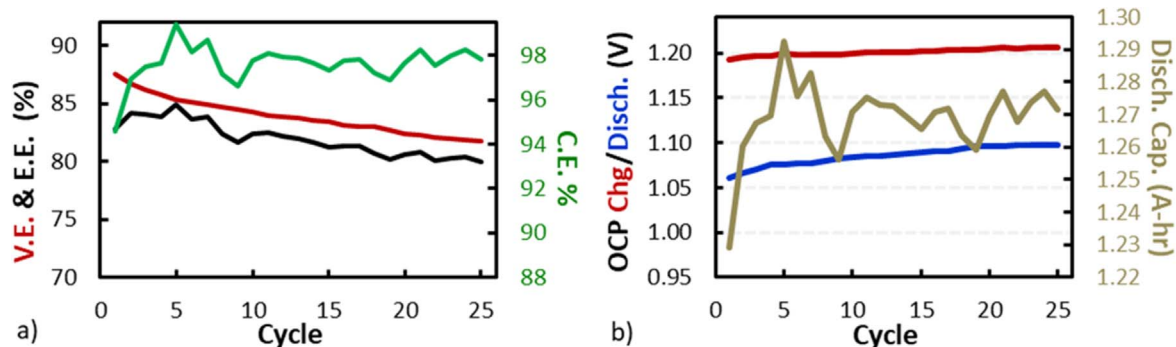
Figure 5. Ni-free metal-contact cell (2× Co-decorated Carbon paper A || AR-Na N115 || DW SS 316 || SS FF) with 30 ml of battery solutions using 2.7 M active material concentrations: (a) cycling efficiencies, (b) OCP collected at the end of change and discharge.

mesh that is largely incompressible. The mesh's incompressibility becomes apparent after cell deconstruction—cycled cells show evidence of pulverization of the softer graphite flow field. This is not observed in the Ni foam cell since the Ni foam compresses more easily. Increased surface area of this oxidizable material can explain both the lower, and decreasing, CE, as well as the increasing OCP— any regeneration of permanganate from manganate generated chemically, rather than electrochemically, corresponds to higher SOCs, and more extreme potentials, in the opposing pS electrolyte. One way to avoid the poor performance of the metal/graphite interface is by eliminating the graphite material completely to create a metal/metal interface.

A metal-contact cell was built with the same components as the Ni-free cell, except that the graphite flow plate has been replaced with a SS 316 flow plate machined to the same specifications. At the beginning of life, the metal contact cell shows a similar 87% VE (vs 88%), but a higher CE at 98% (vs 94%). Similar to the graphite-contact Ni-free cell, the VE decays 4% with cycling. However, cycling does not cause CE decay in the metal-contact cell and the CE remains stable at its elevated levels showing early signs affirming the move from the softer graphite flow plate material. Furthermore, the OCP hold data in Fig. 5b shows a return to similar rates of increase in the OCP hold data with cycling.

Full cell performance with expanded nafion membrane.—Beyond electrodes and their contact resistance, the membrane plays a vital role in flow battery systems. Higher ionic conductivity membranes allow flow battery cells to cycle with higher VE and achieve higher peak power density; however, these may also enable higher crossover rates and lower CE.[28] The boiled N115 membrane (B-Na N115), prepared by boiling in D.I. water for 1 h before sodiating by soaking in 3 M NaOH for 3+ days, delivers higher conductivity flow battery cells than the AR-Na N115. Boiling PFSA membranes is a common pre-treatment used to swell the membranes and allow increased solution uptake and subsequent conductivity. These benefits are probably not permanent, however, as differently pre-treated membranes eventually relaxed to similar performance levels after extended cycling with acidic flow battery solutions.[19]

The expanded membrane cell was built with all same components as the original Ni-free cell, except with the membrane B-Na N115. The expanded membrane cell shows 2.2% higher VE during the cycling test than the cell using AR-Na N115 (Fig. 6a). The OCPs of the expanded membrane cell after each cycles' charge and discharge steps were also lower than the AR-Na N115 cell, indicating increased self-discharge due to the higher crossover through the more conductive, but more permeable membrane (Fig. 6b). The VE shows a similar decay tendency as the original Ni-free, AR-Na N115 membrane cell, indicating both cells experience the same performance loss mechanisms. This agrees with expectations since both cells used the same electrode materials and graphite flow field materials.

The polarization curve shown in Fig. 6c shows the drastic improvement in power density capabilities by using the more conductive membrane. The more conductive membrane drops the full cell resistance to 1.6 Ω-cm^2 for a 33% improvement in power capabilities from the Ni-free cell and 44% improvement over the baseline Ni foam cell. Such improvements would have positive real-world effects by reducing the cost of reactor components in a system by the same amount while operating at a similar EE target of approximately 80%.

The expanded B-Na N115 cell showed a substantially lower CE, however, of 90% which is in agreement with the higher reactant permeability expected from an expanded Nafion membrane. The CE of the cell with expanded membrane looks stable, if not increasing. The increasing CE likely arises at least partially from the contraction of the polymer membrane back towards an equilibrium state for the strongly alkaline, highly concentrated conditions at 50 °C.

Model analysis.—To further understand the performance bottle-necks of the polysulfide-permanganate RFB, a computational model was developed. First, the model was fit to each of the DHC experiments as shown in Fig. S1 by varying the product of the specific surface area a and the exchange current density i_0 for each DHC. The model fits quantify the impact of the cobalt catalyst decorating the carbon paper, showing a factor of 40 increase in the product ai_0 from 0.08 to 3.2 A cm^{-3}.

A full cell model was constructed using polysulfide electrode parameters on the negative side, permanganate electrode parameters on the positive side, and the fitted ai_0 values for each respective electrode, effectively combining the two double half cell models into a full cell model. Using a voltage breakdown approach, this model allows for quantification of kinetic and Ohmic voltage losses in the cell, as shown in Fig. 7. The contributions of each voltage loss mechanism to the cell ASR are given in Table III. Notably, membrane ohmic losses constitute a significant portion of overall voltage losses in the cell, highlighting the critical need for thin, selective, high-conductivity RFB membranes. Mass transport losses are not apparent due to the high concentrations of reactants, rapid flow rates, and interdigitated flowfields used in the cell.

Although combining the DHC models should result in fitting the full cell data without additional adjustments, two additional effects were needed to accurately reproduce the experimental data. First, an offset was added to the open-circuit voltage to account for the effects of polysulfide speciation on the electrode potential. Second, an additional voltage loss equivalent to an Ohmic resistance of 0.69 Ω cm^2 was added to the model to match the slope of the experimental polarization curve, as shown by the orange-colored wedge of the voltage breakdown in Fig. 7. The origin of this voltage loss is unclear; two likely contributors are increases in membrane or cell resistance caused by the precipitation of crossover products, or slower kinetics than modeled due to asymmetry in the reaction kinetics. Future work will focus on determining the cause(s) of this voltage loss so that it can be minimized.
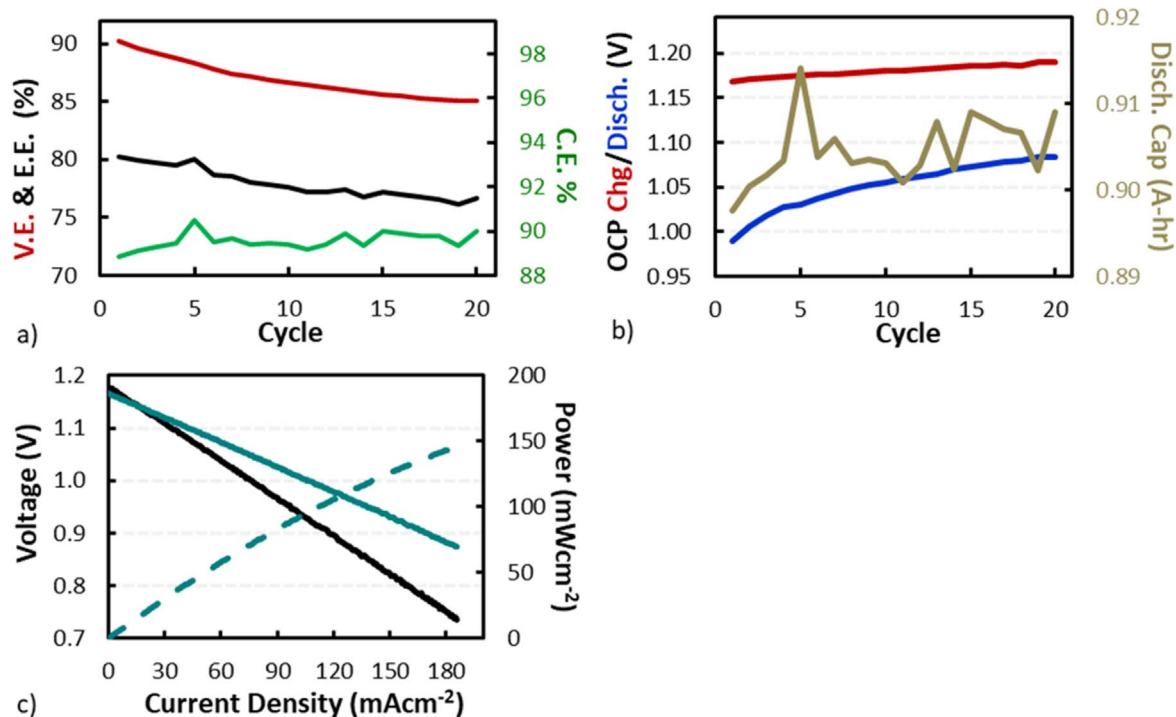
Figure 6. Ni-free Expanded N115 cell (2× Co-decorated Carbon paper A || B-Na N115 || DW SS 316 || SS FF) run with 30 ml of battery solutions using 2.1 M active material concentrations: (a) cycling efficiencies, (b) OCP collected at the end of change and discharge, and (c) polarization curve at 50% SOC (green) compared to polarization curve collected from cell built with AR-Na-N115 (black).
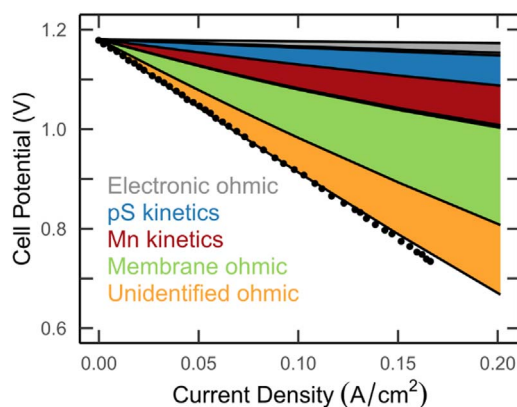

Figure 7. Simulated polarization curve of the pS-Mn RFB during discharge compared to the experimental data. A voltage breakdown is overlaid illustrating the main causes of voltage loss in the cell.

Table III. Equivalent ASR values for each of the voltage loss sources listed in Fig. 6.

Voltage Loss Source	ASR ($\Omega\ cm^2$)
Electronic ohmic	0.12
Polysulfide kinetics	0.31
Permanganate kinetics	0.42
Membrane ohmic	0.97
Unidentified ohmic	0.69

Conclusions

The new sulfur-manganese flow battery chemistry developed here uses low cost active materials that can enable long duration energy storage systems. As reported previously, the strongly alkaline conditions allow stable operation of the disulfide to tetrasulfide polysulfide chainlengths as well as the permanganate-manganate redox couple. Although the formal reaction potentials suggest a cell voltage of 1.1 V, cells at 50% SOC deliver an OCP near 1.2 V, which is corroborated by polysulfide speciation models. This cell voltage, combined with 2.7 M battery solutions give an electrolyte energy density of 43 Wh l^{-1}. A rigorous assessment of material stability at ambient and elevated temperatures identified materials compatible with the strongly oxidizing manganese couple and eliminated some commonly used cell wetted materials from use.

Baseline cells were tested with nickel foam electrodes because of promising results achieved with them in prior polysulfide systems. The Ni-based cells show promising performance at elevated temperatures delivering a cell resistance of 2.7 Ω-cm^2. Alternative electrodes were sought that improved or maintained performance, but used more conventional materials. Co-decorated carbon paper improved polysulfide reaction kinetics significantly and high surface area stainless steel mesh maintained similar performance with a less critical material and simpler construction. Paired together the two advanced electrodes offered an improved cell resistance, 11% lower at 2.4 Ω-cm^2. Further decreases in cell resistance are achieved by separating the advanced electrodes with an expanded Nafion 115 membrane, which has a more porous and more highly conductive structure and enables a polarization resistance of 1.6 Ω-cm^2, or a 44% improvement from the baseline cell. This highlights the relative importance of membrane resistance compared to electrode kinetics at this stage of S-Mn flow battery development.

While the use of a more conductive expanded membrane can improve full cell performance, modeling efforts indicate room for other resistance improvements rather than using membrane pre-treatments that increase conductivity, but also permeability. The full cell model, informed by half-cell data, indicates the presence an unexplained 0.7 Ω cm^2 resistance. Identifying the source of this resistance, and eliminating it, can give similar power performance improvements as the pre-treated membrane.

The S-Mn flow battery system concept has many opportunities for substantial improvements. Most important for any practical system is understanding and resolving the underlying phenomena of the

performance fade observed with cycling. Any performance fade reduces the utility of the system and can outweigh the cost benefits from using inexpensive active materials. Other areas of improvement are more germane to flow batteries such as identifying separators with high ionic conductivity, but lower active material permeability. While these hurdles remain, the promise of high energy density and low battery solution costs make the S-Mn system attractive for further development.

ORCID

Michael R. Gerhardt https://orcid.org/0000-0002-1272-3607
Adam Z. Weber https://orcid.org/0000-0002-7749-1624
Mike L. Perry https://orcid.org/0000-0003-3313-8498
James D. Saraidaridis https://orcid.org/0000-0002-9678-5505

References

1. M. Arbabzadeh, R. Sioshansi, J. X. Johnson, and G. A. Keoleian, "The role of energy storage in deep decarbonization of electricity production." *Nat. Commun.*, **10**, 3413 (2019).
2. Sandia (2020), DOE Global Energy Storage Database (Sandia National Laboratories) https://www.sandia.gov/ess-ssl/global-energy-storage-database/.
3. *Energy Storage Grand Challenge: Energy Storage Market Report*; U.S. Department of Energy: December 2020.
4. M. Padilla (2020), Joint Long Duration Storage Request for Offers.Silicon Valley Clean Energy, https://www.svcleanenergy.org/news/california-community-choice-aggregators-issue-request-for-long-duration-storage/.
5. P. Albertus, J. S. Manser, and S. Litzelman, "Long-duration electricity storage applications, economics, and technologies." *Joule*, **4**, 21 (2020).
6. C. N. Sun, M. M. Mench, and T. A. Zawodzinski, "High performance redox flow batteries: an analysis of the upper performance limits of flow batteries using non-aqueous solvents." *Electrochim. Acta*, **237**, 199 (2017).
7. M. L. Perry, R. M. Darling, and R. Zaffou, "High power density redox flow battery cells." *ECS Trans.*, **53**, 7 (2013).
8. C. Wadia, P. Albertus, and V. Srinivasan, "Resource constraints on the battery energy storage potential for grid and transportation applications." *J. Power Sources*, **196**, 1593 (2011).
9. *Sulfur Data Sheet—Mineral Commodity Summaries 2020*, U.S. Geological Survey (2020).
10. *Manganese Data Sheet—Mineral Commodity Summaries 2020*, U.S. Geological Survey (2020).
11. *Vanadium Data Sheet—Mineral Commodity Summaries*, U.S. Geological Survey (2020).
12. G. H. Kelsall and I. Thompson, "Redox chemistry of H2S oxidation in the British gas stretford process part I: thermodynamics of sulphur-water systems at 298 K." *J. Appl. Electrochem.*, **23**, 279 (1993).
13. M. Pourbaix, *Atlas of Electrochemical Equilibria In Aqueous Solutions.* (National Association of Corrosion Engineers, Houston, Texas) (1974).
14. A. N. Colli, P. Peljo, and H. H. Girault, "High energy density $MnO_4-/MnO42-$ redox couple for alkaline redox flow batteries." *Chem. Commun.*, **52**, 14039 (2016).
15. C. Liu, X. Chi, J. Huang, and Y. Liu, "A high-voltage rechargeable alkaline Zn–MnO_4- battery with enhanced stability achieved by highly reversible $MnO_4-/MnO42-$ redox pair." *Materials Today Energy*, **20**, 100680 (2021).
16. S. Kim, T. B. Tighe, B. Schwenzer, J. Yan, J. Zhang, J. Liu, Z. Yang, and M. A. Hickner, "Chemical and mechanical degradation of sulfonated poly(sulfone) membranes in vanadium redox flow batteries." *J. Appl. Electrochem.*, **41**, 1201 (2011).
17. R. M. Darling and M. L. Perry, "The influence of electrode and channel configurations on flow battery performance." *J. Electrochem. Soc.*, **161**, A1381 (2014).
18. R. M. Darling, A. Z. Weber, M. C. Tucker, and M. L. Perry, "The influence of electric field on crossover in redox-flow batteries." *J. Electrochem. Soc.*, **163**, A5014 (2015).
19. W. Xie, R. M. Darling, and M. L. Perry, "Processing and pretreatment effects on vanadium transport in nafion membranes." *J. Electrochem. Soc.*, **163**, A5084 (2016).
20. R. M. Darling, J. D. Saraidaridis, C. Shovlin, and M. Fortin, "Transference numbers of vanadium cations in nafion." *J. Electrochem. Soc.*, **167**, 020529 (2020).
21. H. Zhou, H. Zhang, P. Zhao, and B. Yi, "Novel cobalt coated carbon felt as high performance negative electrode in sodium polysulfide/bromine redox flow battery." *Electrochemistry*, **74**, 296 (2006).
22. M. R. Gerhardt, A. A. Wong, and M. J. Aziz, "The effect of interdigitated channel and land dimensions on flow cell performance." *J. Electrochem. Soc.*, **165**, A2625 (2018).
23. L. H. Thaller, *Electrochemical cell for rebalancing redoxflow system*, 4,159,366 (1979).
24. C. Fujimoto, S. Kim, R. Stains, X. Wei, L. Li, and Z. G. Yang, "Vanadium redox flow battery efficiency and durability studies of sulfonated diels alder poly (phenylene)s." *Electrochem. Commun.*, **20**, 48 (2012).
25. P. Zhao, H. Zhang, H. Zhou, and B. Yi, "Nickel foam and carbon felt applications for sodium polysulfide/bromine redox flow battery electrodes." *Electrochim. Acta*, **51**, 1091 (2005).
26. L. Su, A. F. Badel, C. Cao, J. J. Hinricher, and F. R. Brushett, "Toward an inexpensive aqueous polysulfide–polyiodide redox flow battery." *Ind. Eng. Chem. Res.*, **56**, 9783 (2017).
27. Q. Chen, M. R. Gerhardt, and M. J. Aziz, "Dissection of the voltage losses of an acidic quinone redox flow battery." *J. Electrochem. Soc.*, **164**, A1126 (2017).
28. M. L. Perry, J. D. Saraidaridis, and R. M. Darling, "Crossover mitigation strategies for redox-flow batteries." *Current Opinion in Electrochemistry*, **21**, 311 (2020).